

Membrane Rigidity-Tunable Fusogenic Nanosensor for High Throughput Detection of Fusion-Competent Influenza A Virus

Chaewon Park, Eunjung Kim, Geunseon Park, Byoung Choul Kim, Srivithya Vellampatti, Jong-Woo Lim, Sojeong Lee, Soohyun Chung, Sung-Hoon Jun, Sangyoon Lee, Sajid Ali, Minjoo Yeom, Daesub Song,* and Seungjoo Haam*

The emergence of fatal viruses that pose continuous threats to global health has fueled the intense effort to develop direct, accurate, and high-throughput virus detection platforms. Current diagnostic methods, including qPCR and rapid antigen tests, indicate how much of the virus is present, whether small fragments or whole viruses. However, these methods do not indicate the probability of the virus to be active, capable of interacting with host cells and initiating the infection cycle. Herein, a sialic acid-presenting fusogenic liposome (sLipo–Chol) nanosensor with purposefully modulated membrane rigidity to rapidly detect the fusion-competent influenza A virus (IAV) is developed. This nanosensor possesses virus-specific features, including hemagglutinin (HA) binding and HA-mediated membrane fusion. It is explored how the fusogenic capability of sLipo–Chol with different membrane rigidities impacts their sensing performance by integrating Förster resonance energy transfer (FRET) pairs into the bilayers. The addition of an intact virus led to instant FRET signal changes, thus enabling the direct detection of diverse IAV subtypes—even in avian fecal samples—within an hour at room temperature. Therefore, the sensing approach, with an understanding of the cellular pathogenesis of influenza viruses, will aid in developing bioinspired nanomaterials for evolution into nanosystems to detect infection-competent viruses.

(MERS-CoV), and Ebola virus. Now, the unprecedented outbreak of coronavirus disease 2019 (COVID-19) caused by SARS-CoV-2, as the first example of unknown pathogens (referred to as Disease X), is an ongoing threat to humanity, imposing devastating impacts on societies and economies globally.^[1,2] The enormous efforts in preventive strategies to mitigate the spread of viruses early in the outbreak have been pursued to develop advanced diagnostic technologies that can be readily applicable for emerging target viruses and implement well-organized widespread testing.

Among the widely used conventional diagnostic tests for virus infection, quantitative polymerase chain reaction (qPCR) has been considered the gold standard method due to its high analytical sensitivity and specificity. However, it requires intensive sample preparation and amplification steps, which impedes large-scale field testing of various types of specimens. Alternatively, rapid immunological tests provide quick sample-to-answer results

with the potential of point-of-care testing, but compared to qPCR, they present limited use for diagnosis due to their moderate sensitivity (50%–70%).^[3] More critically, these qPCR and rapid immunological tests identify the presence of viral genetic materials and antigens but not intact viruses. Thus, detecting viral materials using qPCR and rapid detection kits poses

1. Introduction

In the past two decades, emerging infectious viruses have been a continuous threat to global health, including novel influenza A (H1N1) virus, severe acute respiratory syndrome coronavirus (SARS-CoV), Middle East respiratory syndrome coronavirus

C. Park, G. Park, S. Lee, S. Chung, S. Lee, S. Haam
Department of Chemical and Biomolecular Engineering
Yonsei University
Seoul 03722, Republic of Korea
E-mail: haam@yonsei.ac.kr

E. Kim, B. C. Kim, S. Vellampatti
Department of Bioengineering and Nano-Bioengineering
Incheon National University
Incheon 22012, Republic of Korea

 The ORCID identification number(s) for the author(s) of this article can be found under <https://doi.org/10.1002/adfm.202214603>.

DOI: 10.1002/adfm.202214603

J.-W. Lim, M. Yeom, D. Song
College of Veterinary Medicine and Research Institute for Veterinary Science
Seoul National University
Seoul 08826, Republic of Korea
E-mail: sds@snu.ac.kr

S.-H. Jun
Electron Microscopy & Spectroscopy Team
Korea Basic Science Institute
Chungbuk 28119, Republic of Korea

S. Ali
Department of Electrical and Computer Engineering
Sungkyunkwan University
Suwon 16419, Republic of Korea

false-positive risks since these methods cannot differentiate between intact infectious viruses (active virus) and leftover fragments from infection (inactive or decomposed virus) that have already been neutralized by a person's antibodies.^[4,5] This could further overestimate the number of viruses present in a sample, which could be a potential cause for a false-positive diagnostic result with a person experiencing prolonged viral shedding after recovery. Low levels of viral RNA detected by qPCR cannot be equated with infectivity unless infectious viruses are isolated and identified using laboratory viral cultures (or plaque assays). However, the culture-based method is impractical for early diagnosis and identification of viral infection because it takes 5–9 days to obtain available results.

Nanosensor technologies to detect infectious viruses, such as resistive-pulse sensing and nanopore sequencing, have been reported.^[6–9] Resistive-pulse methods using solid-state nanopores can directly detect single virus particles by trapping the virus within the nanopore and measuring the change in electric current, providing fast results and improved sensitivity. However, to capture and identify specific viruses, the nanopore surface should be modified with biorecognition molecules such as peptides, antibodies, and aptamers. Additional steps are required to optimize the size and shape of the nanopores and control membrane thickness to obtain reproducible and accurate results with high sensitivity. Nanopore sequencing also offers a fast and precise method for identifying viral strains or mutations because it allows for real-time sequencing at the single-base level. However, like traditional sequencing techniques, it requires nucleic acid extraction and purification and library preparation, which is time-consuming and labor-intensive, making it more suitable for viral genome identification than clinical diagnosis in pandemic situations.

In contrast to viral RNA and antigen fragments, intact virus particles are capable of entering the host cell by attachment to cell surface receptors and fusion with host cell membranes, followed by the release of the viral genome for replication.^[10,11] Such virus entry depends on specific viral envelop glycoprotein-mediated binding to host cell receptors and membrane fusion, which can be triggered by pH changes, cations (e.g., calcium and potassium ions), and enzymatic cleavages.^[12,13] By closely mimicking the surface binding and entry mechanisms of an enveloped virus, host cell-resembling nanoparticles can be used as biosensors to detect intact virus particles.^[14] Notably, the virus-host cell membrane fusion involves reorganizing and merging two thermodynamically stable and separate lipid membranes into a single continuous bilayer, inducing simultaneous changes in the structural and mechanical properties of membranes.^[15] Altering membrane composition has multifactorial effects on fusion by manipulating the bilayer structures and spatial organization. In this context, cholesterol is of particular interest in regulating the efficiency and rate of fusion, which are directly implicated in the entry of many enveloped viruses, such as influenza, human immune deficiency virus, and coronavirus.^[16] Depletion of cholesterol from both host and/or viral membranes has also been shown to disrupt fusion kinetics.^[17,18] Therefore, this suggests that the tuning of membrane rigidity and fluidity of detection nanoplateforms is able to enhance detection performance by maximizing fusion kinetics.

In this study, we developed a fusogenic nanosensor for rapid, accurate, and high throughput detection of fusion-competent intact influenza A virus (IAV). To the best of our knowledge, this study constitutes the first example of a membrane rigidity modulated Förster resonance energy transfer (FRET) nanosensor for virus detection. Our fusogenic nanosensor is based on sialic acid-presenting liposomes (sLipo–Chol) resembling viral entry dynamics through specific binding to the virus and hemagglutinin (HA)-mediated fusion. We screened the effects of membrane rigidity on the sensor's performance by assessing the fusion kinetics of IAV with sLipo–Chol containing FRET dyes (DiO donor/DiI acceptor) and different contents of cholesterol (0, 33, and 50 mol%) in the lipid bilayer (**Figure 1**). The fusion kinetics was evaluated by measuring the FRET signals at bulk or a single-particle level to obtain detailed kinetic information about sLipo–Chol nanosensors with the virus to the mole fraction of cholesterol in the liposome membrane. We also demonstrated that membrane rigidity and fluidity could be leveraged to enhance the fusion efficiency of the nanosensors, leading to amplified fluorescence signals in the presence of target viruses. To do this, the activated IAV was introduced to bind to the surface of the nanosensors through interactions between HA and sialic acid residues, and fusion was initiated with the acidic buffer (pH 5.2). This fusion process promoted the fusion of sLipo–Chol nanosensors and virus membranes and allowed diffusion of the entrapped dye molecules into the extended membranes, producing FRET signal changes from high to low FRET over time. Thus, the liposomes with less membrane rigidity exhibited susceptible fusion activity against the activated virus, reaching a lower detection limit than those with stiffer membranes. In addition, this fusogenic nanosensor showed high sensitivity and specificity toward diverse IAV subtypes by mixing at room temperature, even in avian fecal samples, indicating the reliability and robustness of its sensing performance. Thus, the various IAV subtypes that our sensor detects, relying on its fusion activity, are extensively applicable to the direct detection of different infectious viruses in a straightforward and high-throughput manner.

2. Results and Discussion

2.1. Preparation and Characterization of Fusogenic sLipo–Chol Nanosensors

To sense the whole influenza virus, we designed biomimetic sialic acid-bearing liposomes with cholesterol (sLipo–Chol) that allow selective recognition and binding to viral hemagglutinin (HA) and instant production of readable signals upon membrane fusion with viruses. The sLipo–Chol was prepared using the conventional lipid film hydration and extrusion method. The lipid membranes mainly comprised two phospholipids, DSPC (18:0 PC, 1,2-distearoyl-*sn*-glycero-3-phosphocholine) and DSPS (18:0 PS, 1,2-distearoyl-*sn*-glycero-3-phospho-L-serine), whose glass transition temperatures are above 50 °C, forming a solid-ordered phase in a hydrated state.^[19] Poly(ethylene) glycol (PEG)-modified DSPE (1,2-distearoyl-*sn*-glycero-3-phosphoethanolamine) (DSPE–PEG) and total ganglioside (TG) extracts (from the porcine brain) containing sialic acid residues in the

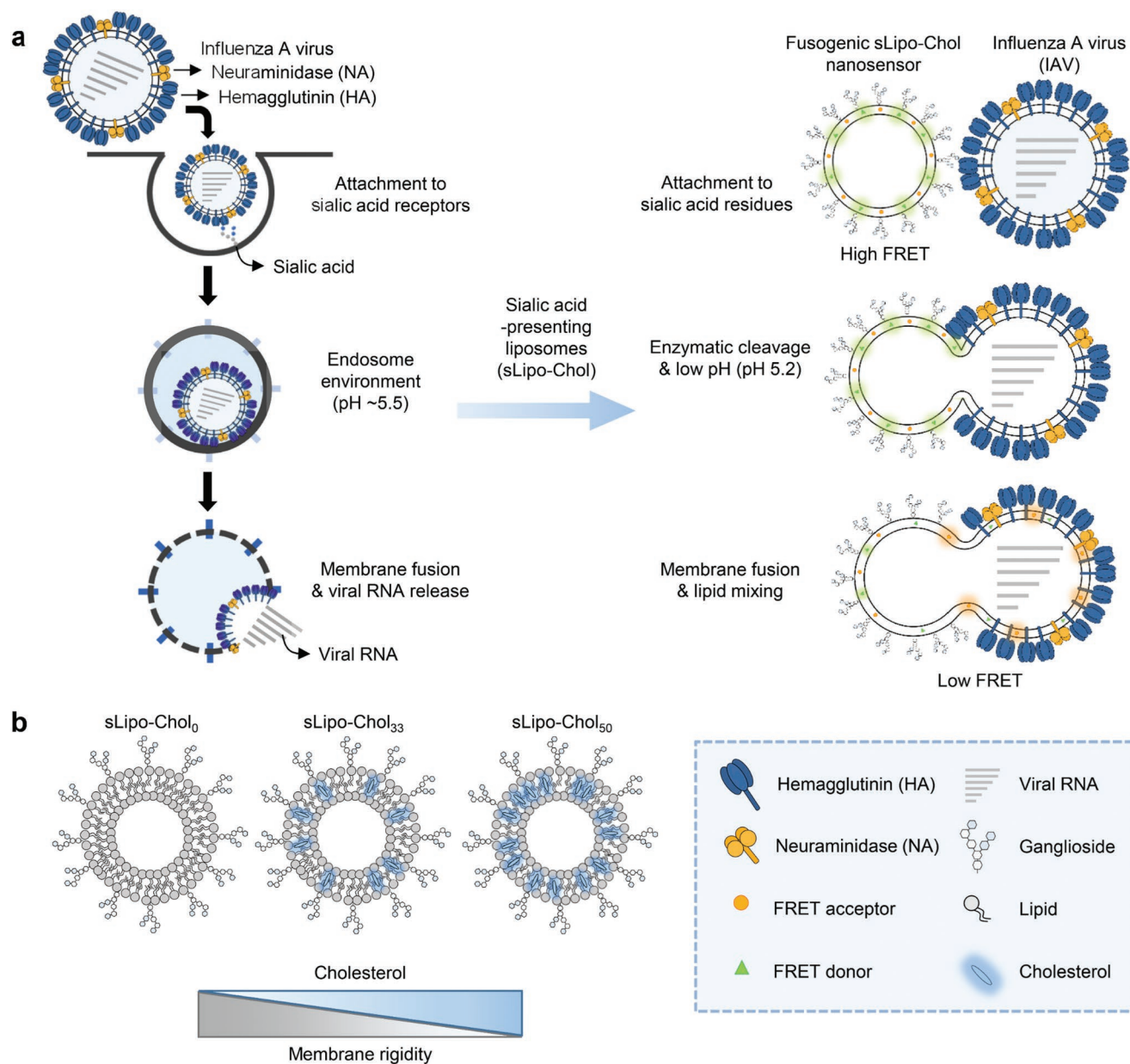


Figure 1. IAV detection approach with a host cell-mimicking fusogenic nanosensor. a) Schematic of the infection cycle of IAV and the proposed virus detection using sialic acid-presenting liposomes with various cholesterol contents (sLipo-Chol nanosensors) that render binding capacity to HA protein. The process of sialic acid anchoring and subsequent membrane fusion of sLipo-Chol nanosensors and virus membranes through proteolytic cleavage of HA fusion peptides under acidic pH was shown. b) Schematic of three types of sLipo-Chol nanosensors with decreasing membrane rigidity prepared by inserting increasing molar ratios of cholesterol to sLipo-Chol (sLipo-Chol₀, sLipo-Chol₃₃, and sLipo-Chol₅₀).

glycan chain were further mixed with DSPC and DSPS to formulate lipid films with a DSPC:DSPS:DSPE-PEG:TG molar ratio of 1:1:0.15:0.06. We also considered including cholesterol in the lipid composition, as it plays a critical role in regulating the physical properties of native lipid bilayers, including membrane rigidity, fluidity, and thermodynamic phase.^[20] To tune the membrane rigidity of sLipo-Chol, we added cholesterol to the lipid mixtures in increasing amounts (0, 33, and 50 mol%). The formed lipid vesicles were extensively extruded at least 51 times through a polycarbonate membrane with a 100 nm pore size to obtain a monodisperse, unilamellar

liposome population. The extruded sLipo-Chol were referred to as sLipo-Chol₀, sLipo-Chol₃₃, and sLipo-Chol₅₀, depending on the cholesterol content.

We first analyzed their morphology and size distribution using transmission electron microscopy (TEM) and dynamic light scattering (DLS). As depicted in **Figure 2a,b**, three sLipo-Chol showed unilamellar spherical vesicles with mean hydrodynamic diameters of 109.1 ± 6.1 , 98.7 ± 3.2 , and 102.0 ± 4.0 nm for sLipo-Chol₀, sLipo-Chol₃₃, and sLipo-Chol₅₀, respectively. These liposomes also displayed no appreciable differences in zeta potential (-20.2 ± 6.3 , -22.1 ± 3.2 , and -22.2 ± 4.1 mV

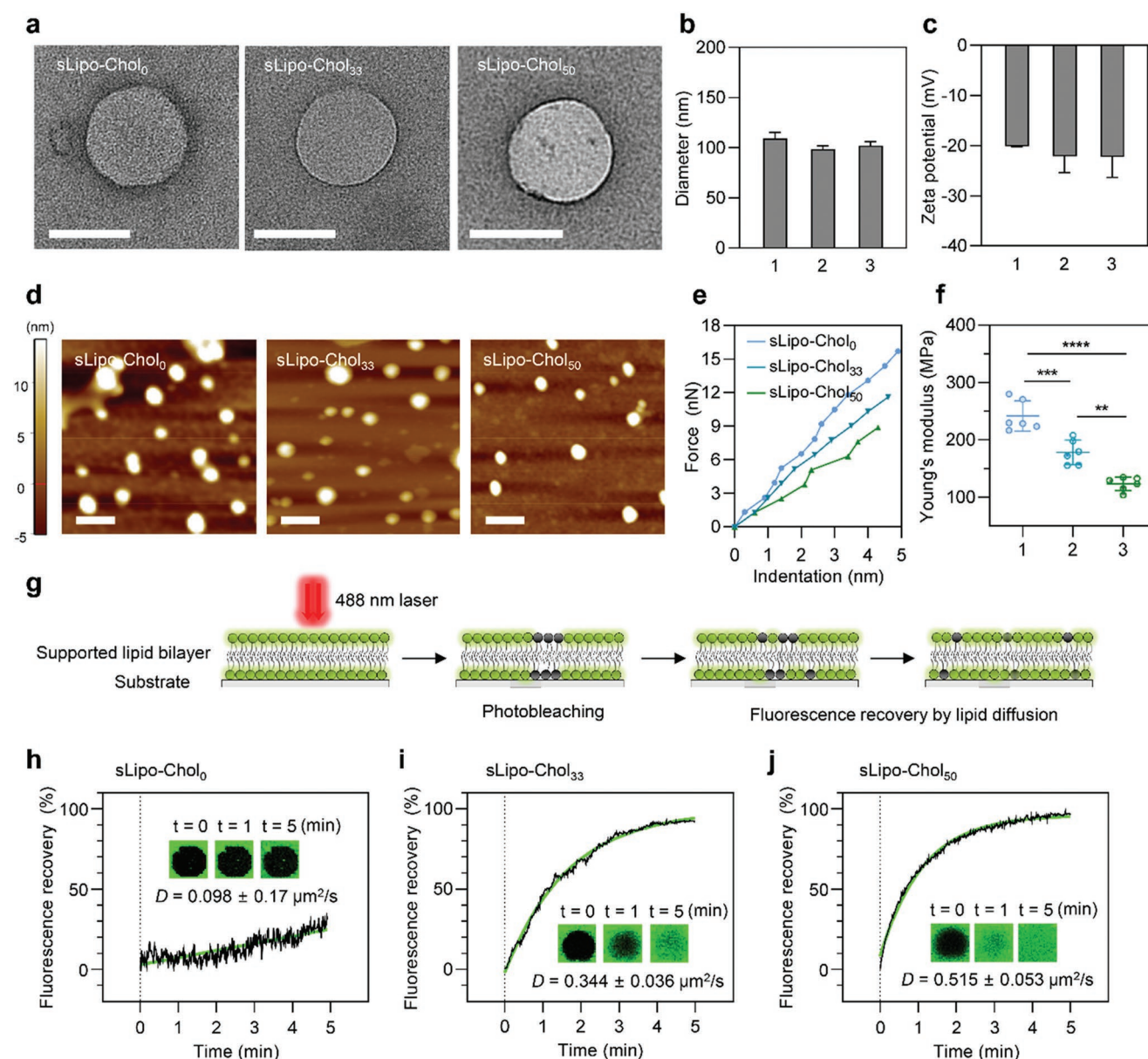


Figure 2. Characterization of sLipo-Chol nanosensors. a) Representative TEM images of sLipo-Chol stained negatively with 3% (w/v) neutral phosphotungstic acid solution. Scale bar: 100 nm. b) Hydrodynamic diameters and c) zeta potentials of sLipo-Chol determined by DLS. Data represents mean ± standard deviation (n = 3). d) Representative AFM topography images of sLipo-Chol with contact mode measurements, e) force-indentation depth curves to determine Young's modulus of individual sLipo-Chol, and f) average Young's modulus values calculated with the Hertzian model. Data represents mean ± standard deviation (n = 6). Sample 1, sLipo-Chol₀; Sample 2, sLipo-Chol₃₃; Sample 3, sLipo-Chol₅₀. One-way analysis of variance was used for statistical analysis of the calculated Young's modulus between sLipo-Chol (****p < 0.0001, ***p < 0.001, and **p < 0.01). g) Schematic of FRAP measurements of the supported lipid bilayer derived from sLipo-Chol on the substrate. After photobleaching with a 488 nm laser, the fluorescence images and intensities of the region of interest were obtained for 5 min. FRAP curves of the supported lipid bilayer formed with h) sLipo-Chol₀, i) sLipo-Chol₃₃, and j) sLipo-Chol₅₀. Fitting curves are drawn in green, and diffusion coefficients (D) for each curve were obtained from fitting results using a nonlinear one-phase association model. Fluorescence confocal images of the region of interest are shown in the inset over the acquisition time.

for sLipo-Chol₀, sLipo-Chol₃₃, and sLipo-Chol₅₀, respectively (Figure 2c).

The mechanical properties of lipid membranes determine various aspects of liposome behavior, such as their deformation, stability, fusion, and budding processes.^[21] To characterize and tailor the deformability and fusion capacity of sLipo-Chol, we assessed their membrane rigidity by measuring Young's

modulus of individual sLipo-Chol with topology imaging using atomic force microscopy (AFM) at the nanoscale. The cantilever probe used in AFM measurements was in direct contact with each liposome. It generates its elastic deformation under probe compression, which can be used to calculate Young's modulus based on the force-distance curve. The AFM images of sLipo-Chol₀, sLipo-Chol₃₃, and sLipo-Chol₅₀ immobilized on the

mica substrate showed spherical nanoparticles with sizes of ≈ 100 nm, which is a good agreement with the DLS and TEM results (Figure 2d). We further evaluated the force versus indentation depth curves with AFM for quantitative Young's modulus measurements of each formulation (Figure 2e; Figure S1, Supporting Information). Given the nonelastic nature of liposomes, we attempted to obtain their elastic behavior by carefully pressing the cantilever tip, inducing a small degree of deformation (indentation depth: ≈ 5 nm), and then we calculated Young's modulus using the Hertzian model.^[22] The average Young's modulus was 241.4 ± 26.8 , 178.6 ± 21.6 , and 123.1 ± 11.9 MPa for sLipo-Chol₀, sLipo-Chol₃₃, and sLipo-Chol₅₀, respectively, with a statistically significant difference, indicating that the inclusion of cholesterol in saturated lipid bilayers induced an eventual decrease in lipid membrane rigidity. This is consistent with the previous observations that lipid phase ordering (such as solid-ordered, liquid-ordered, and liquid-disordered phases) likely plays an important role in the bending rigidity of nano-sized liposomes.^[15] This is supported by the fact that increasing cholesterol content in the liposome membrane consisting of saturated PC lipids showed a thermodynamic transition from a solid-ordered to a liquid-ordered phase and decreased their membrane bending rigidity.^[19,23] Thus, sLipo-Chol₃₃ and sLipo-Chol₅₀, predominantly composed of lipids with two saturated alkyl chains (DSPC and DSPS) and cholesterol, became less rigid compared to sLipo-Chol₀ without cholesterol due to the cholesterol-induced solid-liquid phase transition. Alterations in membrane rigidity are expected to influence the fusion process and diffusion of signaling molecules entrapped within the membrane, contributing to the sensor's reactivity to viruses.

Membrane fluidity is another important dynamic parameter modulating the lipid bilayer environment, which may explain how readily and rapidly the Förster resonance energy transfer (FRET) dye pairs diffuse laterally within the lipid bilayer of sLipo-Chol when fused with the virus. To characterize the fluidity of lipid membranes, we conducted a fluorescence recovery after photobleaching (FRAP) experiment that measures the lateral diffusion rate of a supported lipid bilayer.^[24] For the test, we prepared each sLipo-Chol using a fluorescently labeled lipid and formed a supported lipid bilayer by rupturing the liposomes with an extended length of PEG.^[25] Upon photobleaching of a small region with a 488 nm laser, the fluorescence intensity recovers as unbleached fluorescent lipid molecules diffuse into the photobleached area (Figure 2g). We estimated the diffusion coefficient (D) of sLipo-Chol₀, sLipo-Chol₃₃, and sLipo-Chol₅₀ in supported membranes from the fitted kinetics of fluorescence recovery using the nonlinear one-phase association model.^[26] As shown in Figure 2h–j and Figure S2 (Supporting Information), sLipo-Chol₀ with a densely ordered membrane system resulted in no appreciable recovery upon photobleaching, whereas sLipo-Chol₃₃ and sLipo-Chol₅₀ fully recovered the fluorescence within a few minutes. The diffusion coefficients were estimated to be $D = 0.098$, 0.344 , and $0.515 \mu\text{m}^2 \text{s}^{-1}$ for sLipo-Chol₀, sLipo-Chol₃₃, and sLipo-Chol₅₀, respectively, agreeing with previous studies that more saturated membranes yielded slower diffusion in supported lipid bilayers.^[27]

We further analyzed the degree of membrane fluidity of sLipo-Chol using a Laurdan fluorescent probe, sensitive to

the surrounding environment's polarity and lipid phases, providing insights into membrane fluidity.^[28,29] When Laurdan is incorporated into the membrane, the emission of more fluidic membranes is red-shifted from 450 nm (gel phase) to 510 nm (liquid-ordered phase), which can be quantified by the generalized polarization (GP)-based ratiometric analysis. The GP is calculated from the emission spectra (as described in the Experimental Section), and a low GP value is associated with increased membrane fluidity. As shown in Figure S3a (Supporting Information), Laurdan embedded in sLipo-Chol₃₃ and sLipo-Chol₅₀ underwent redshifts in the fluorescence spectra toward 510 nm, indicating that their membranes are at a more fluidic state than sLipo-Chol₀. The corresponding GP values gradually decreased from 0.613 to 0.444 with increasing cholesterol contents (Figure S3, Supporting Information), demonstrating that cholesterol locally increases the fluidity of saturated lipid membranes. This lipid ordering trend agrees well with FRAP measurements, showing that sLipo-Chol with more fluidic membranes led to faster lipid diffusion.

In addition, we explored the membrane stability of sLipo-Chol to examine whether they could withstand external amphiphilic stimuli that disturb the arrangement and packing of lipids.^[30] This can be correlated to the extent of resistance to membrane deformation. We carried out a solubilization assay using the nonionic surfactant Triton X-100 (Tx-100) (Figure S4a, Supporting Information).^[31,32] We prepared sLipo-Chol containing FRET pairs (DiO donor and DiI acceptor). Note that the initial FRET ratios of sLipo-Chol₀, sLipo-Chol₃₃, and sLipo-Chol₅₀ showed slight variations of 0.764, 0.781, and 0.804, respectively. When treated with 10% (v/v) Tx-100, we observed a sudden decrease in the FRET ratios of sLipo-Chol₃₃ and sLipo-Chol₅₀, while a marginal signal change was observed for sLipo-Chol₀ (Figure S4b, Supporting Information). This tendency indicates that sLipo-Chol₅₀ had a lower degree of membrane resistance against surfactants than sLipo-Chol₀; therefore, we considered sLipo-Chol₅₀ to exhibit the largest stability among other formulations. Hence, from these results along with AFM indentation studies, FRAP experiments, Laurdan assays, and solubilization assays with Tx-100, we can infer that the change in lipid composition altered the mechanical behaviors of the formulated liposomes, giving rise to potential changes in their membrane fusion dynamics with viruses.

2.2. Membrane Fusion Activity Between sLipo-Chol Nanosensors and IAV

Our sensing approach relies on the fusogenic ability of FRET pair-integrated sLipo-Chol (hereafter, referred to as sLipo-Chol nanosensors) that specifically interact with the HA fusion protein of the IAV. The design rationale of the sLipo-Chol nanosensor is to decoy the IAV's biological entry process for infection, involving HA binding to sialic acid groups of host cell surface glycoproteins and HA-triggered membrane fusion. We adopted such sialic acid analogs to the surface of liposomes to enable specific molecular recognition and membrane fusion. We then entrapped FRET pair dyes (DiO as a donor and DiI as an acceptor) in the membrane to induce viral fusion-dependent signal generation. The HA protein of the IAV undergoes

proteolytic cleavage into the two HA subunits (HA1 and HA2), triggered by the host enzyme (trypsin) and subsequent conformational changes in a low pH environment, exposing amphophilic fusion peptides to the target membrane for fusion.^[33] Such enzyme-induced and low pH-induced membrane fusion activity between IAV and host cells provide important insights into the design of a simple and rapid assay for specific and sensitive detection of infection-competent IAV using fusogenic sLipo–Chol nanosensors.

By using confocal microscopy imaging, we first tracked the colocalization of sLipo–Chol nanosensors and IAV. We labeled the nanosensor and virus for imaging with DiO and DiI lipophilic fluorescent dyes, respectively. The virus was activated by pretreatment with trypsin for HA maturation before being added to the nanosensor with an acidic buffer (1.5 M sodium acetate, pH 5.2). Representative images showed that the sLipo–Chol₅₀ nanosensor incubated with activated viruses under an acidic condition displayed predominant colocalization, whereas nonactivated viruses with no acidic buffer showed very few fusion spots with sLipo–Chol₅₀ (Figure S5, Supporting Information). Fluorescence intensity profiles also supported the coexistence of sLipo–Chol₅₀ and activated viruses, demonstrating an enhanced interaction of nanosensors with IAV under specified conditions. This interaction was further confirmed by cryogenic TEM (cryo-TEM), allowing high-resolution examination of a native and hydrated specimen maintained in a test buffer condition. As shown in Figure 3a and Figure S6 (Supporting Information), homogeneously dispersed, unilamellar sLipo–Chol₅₀ yielded irregular, large multilamellar liposomes with a heterogeneous size distribution. More interestingly, we observed that multiple nanosensors surrounded a virus, likely to indicate the binding and fusion of nanosensors with IAV at the ensemble level, as depicted in Figure 3b.

Next, we performed a single-particle FRET study using total internal reflection fluorescence (TIRF) microscopy to directly observe the fusion dynamics of individual nanosensors with the activated IAV regarding HA receptor binding, low pH-driven HA conformational changes, and coordinated membrane fusion. The sLipo–Chol₅₀ nanosensor was modified with biotin for immobilization to PEG-passivated substrates through biotin-neutravidin linkages and labeled with DiI (donor). The IAV was labeled with DiD (acceptor). In a typical experiment, we added DiD-labeled IAV and/or acidic buffer to the chamber slide with surface-tethered DiI-labeled nanosensors. With the donor excitation, we recorded the emission intensity of hundreds of nanosensors and IAV through two independent channels for the donor and acceptor while extracting their spatial distribution. The FRET ratio was defined as the relative fluorescence intensity of DiI normalized to the total fluorescence intensity and was analyzed using a custom MATLAB code. As shown in Figure 3c,d, the surface tethered sLipo–Chol₅₀ nanosensors emitted DiI donor signals only with a low FRET ratio (0.01, $n = 376$), whereas the addition of activated IAV to the nanosensors induced an intermediate FRET signal (0.65, $n = 158$). The intermediate FRET ratio reflects close contact between the nanosensor and IAV at neutral pH, indicating that they were arrested at the docked state driven by HA-sialic acid interactions.^[34,35] Note that the HA of IAV was activated by trypsin treatment, which is critical for virus infectivity.^[36,37]

Proteolytic activation of HA involves a transformation of an inactive HA precursor (HA0) into HA1 (receptor binding) and HA2 (membrane fusion) subunits, facilitating translocation of the fusion peptide in HA2 to the target membrane following exposure to low pH.^[38,39] Thus, introducing an acidic buffer to the mixture of nanosensors and activated IAV increased the FRET ratio (0.79, $n = 427$), effectively promoting the fusion event. Consistent with these FRET signal changes, the increase in spot area corresponding to the FRET ratio of individual objects revealed a distinct fusion event at the single-particle resolution, where a significant increase in spot area was found in nanosensors and IAV at low pH (Figure 3e). A representative time trace and the corresponding snapshots of the single fusion event displayed a drastic increase in FRET ratios and instant colocalization of a nanosensor with a virus upon injection of the acidic buffer into the chamber slide (Figure 3f,g). At 40 s, the single-particle FRET signal reached saturation, and the virus fully fused with the nanosensor. Taken together, these analyses indicate that the designed fusogenic nanosensor successfully decoyed the IAV and caused rapid fusion with the viral membrane triggered by acidic pH.

2.3. Detection of IAV with Fusogenic sLipo–Chol Nanosensors

Based on the fusion dynamics, we developed a virus detection assay using sLipo–Chol nanosensors. In this assay, allantoic fluids containing H9N2 IAV were activated with trypsin for 20 min to trigger the HA cleavage and incubated sequentially with sLipo–Chol nanosensors for virus docking. After 20 min, the acidic pH buffer was treated to induce membrane fusion, and the changes in the sLipo–Chol nanosensors from high to low FRET signals were recorded using a laboratory microplate reader. We calculated the FRET ratio changes based on the relative values of the FRET ratios of sLipo–Chol nanosensors treated with virus stocks and 10% (v/v) Tx-100 (as a minimum FRET signal), normalized with respect to the maximal changes of FRET ratios (see Experimental Section for details of calculation). Here a 100% FRET ratio change indicates complete disassembly of the nanosensors due to fusion with viruses.

To examine whether the fusion route of HA binding and acidic pH can specifically prompt detection signals, we compared the FRET ratio changes of the sLipo–Chol₅₀ nanosensor when incubated with an activated virus, 4% formaldehyde-treated denatured virus, and an acidic buffer (Figure S7, Supporting Information). Here, we used formaldehyde to denature surface proteins of IAV, thus generating infection-incompetent viruses.^[40] We also removed any residual formaldehyde through successive centrifugation to prevent possible unintended signal inhibition. In these reactions, the significant FRET ratio response was seen only in the activated virus group, implying that the nanosensors are kinetically stable with virus particles or in the acidic buffer and could potentially discriminate viable virus particles from inactivated or dead viruses. Furthermore, to demonstrate that virus particles with intact viral envelope and conserved HA, rather than single antigen proteins, are essential for sLipo–Chol nanosensor-based detection, we tested the nanosensor and a commercial HA rapid antigen kit using soluble HA protein (purified from A/Hong Kong/483/97 H5N1)

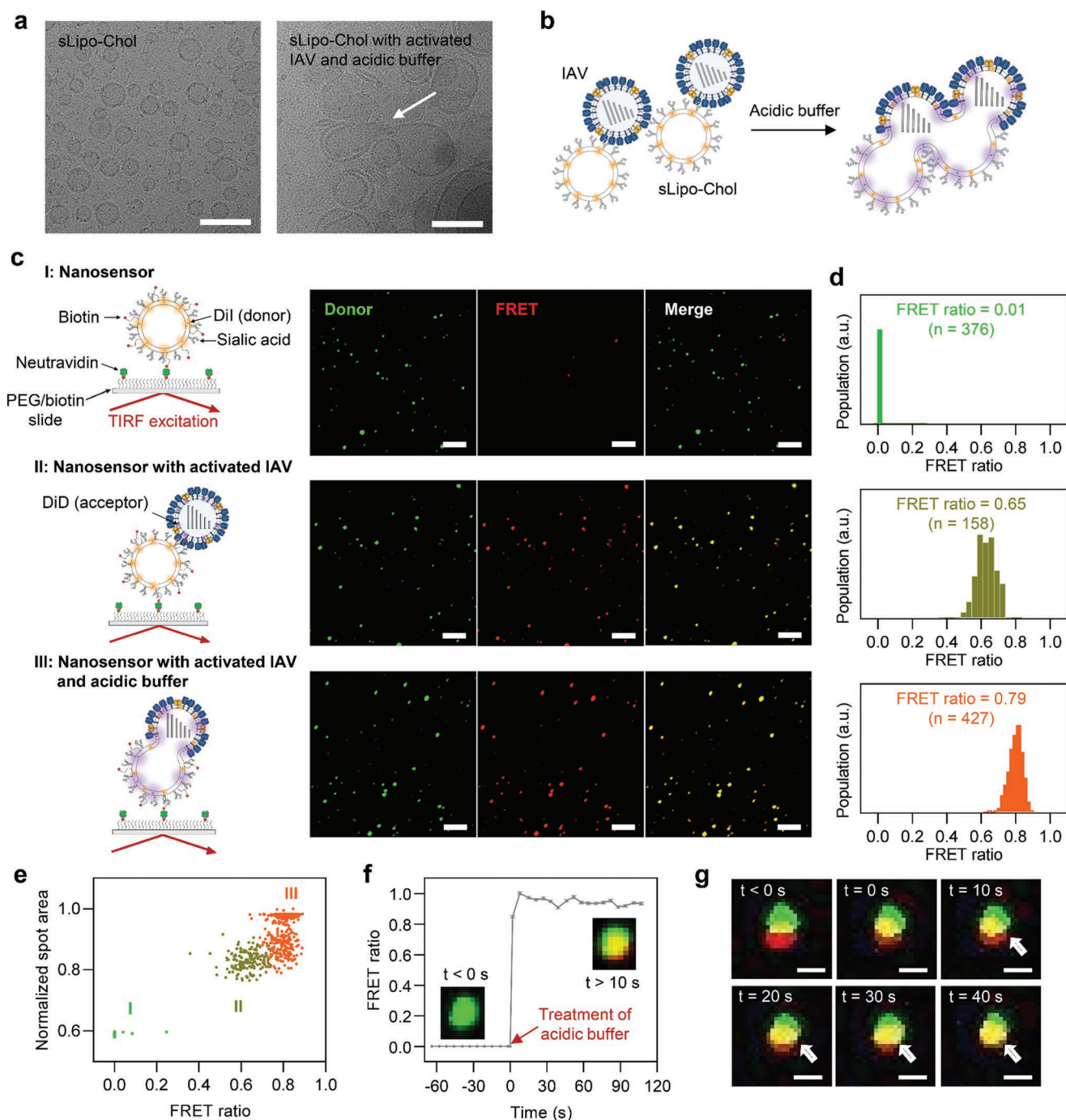


Figure 3. Membrane fusion activity of sLipo-Chol nanosensors with IAV. a) Cryo-TEM images of sLipo-Chol₅₀ (0.05 mg mL⁻¹) without and with the treatment of an activated IAV (10^{3.833} TCID₅₀ mL⁻¹). Scale bar: 200 nm. b) Schematic of membrane fusion between sLipo-Chol and IAV under acidic conditions in a bulk solution. c,d) TIRF microscopy imaging approach for elucidating single-particle membrane fusion of a sLipo-Chol nanosensor with the activated IAV. The nanosensor was labeled with DiI (donor, green) and tethered on PEG-passivated surfaces by biotin-neutravidin interaction. The IAV was labeled with DiD (acceptor, red). c) Representative TIRF images and d) FRET ratio histograms of sLipo-Chol₅₀ nanosensors (I) with non-treatment of IAV and acidic buffer, (II) with the treatment of IAV, and (III) with the treatment of IAV and acidic buffer. The images were captured after adding an acidic buffer. Scale bar: 10 μ m. e) Scatter plot of the FRET ratio versus normalized spot area for each population showing a significant shift in the size distribution of sLipo-Chol nanosensors after treatment with IAV and acidic buffer. f) FRET ratio traces of a single-particle fusion event with $t = 0$ s after adding the acidic buffer. Inset images indicate a single nanosensor (green) in the absence and presence of an activated IAV (red). Data present mean \pm s.d. (n = 5). g) Representative time-lapse TIRF snapshots showing a single-particle fusion event for the nanosensor (green) with an activated IAV (red) before and after treating acidic buffer. The acidic buffer was added at $t = 0$ s. Scale bars: 1 μ m.

as a target sample (Figure S8, Supporting Information). The results showed that the nanosensor exhibited no change in FRET ratio under any treatment condition, whereas the rapid kit showed a clear band indicating the existence of the HA protein in the test line. Thus, the nanosensor can discriminate live infectious viruses from antigen protein fragments.

Next, we screened the effect of the surface charges of nanosensors on interaction with IAV (Figure S9, Supporting Information). From the original constituents of sLipo–Chol₅₀ (DSPC, DSPS, DSPE–PEG, TG, cholesterol), we replaced an anionic DSPS lipid with zwitterionic DSPC or cationic DSTAP (1,2-stearoyl-3-trimethylammonium-propane). The prepared nanosensors from each formulation showed different zeta potentials, including -22.2 ± 4.1 (DSPS, anionic), -11.0 ± 0.4 (DSPC, zwitterionic), and 10.9 ± 1.4 mV (DSTAP, cationic), as expected. After conducting the detection assay, the anionic sLipo–Chol₅₀ nanosensors led to activated virus-specific FRET ratio enhancement, whereas the zwitterionic and cationic nanosensors did not show any significant signal increase among the test groups. This result indicates that negatively charged sLipo–Chol nanosensors are suitable for improving the affinity with the target virus.

Additionally, we prepared another type of sLipo–Chol by replacing saturated lipids (DSPC and DSPS) with unsaturated lipids, including DOPC (1,2-dioleoyl-*sn*-glycero-3-phosphocholine) and DOPS (1,2-dioleoyl-*sn*-glycero-3-phospho-L-serin), to investigate whether the membranes with liquid-ordered and liquid-disordered phases have the potential as a fusogenic nanosensor. Like sLipo–Chol₅₀, the liposome was formed with a DOPC:DOPS:DSPE-PEG:TG:cholesterol molar ratio of 1:1:0.15:0.06:1, referred to as sLipo(u)–Chol₅₀. Since lipid compositions directly impact the lipid membrane rigidity and fluidity, these features of sLipo(u)–Chol₅₀ were assessed by AFM-based indentation study and Laurdan assay and compared with those of sLipo–Chol₅₀. Figures S1 and S2 (Supporting Information) show distinct differences in force-indentation profiles and Laurdan emission spectra between two liposomes, reporting significantly decreased Young's modulus and GP value of sLipo(u)–Chol₅₀ (26.9 ± 3.9 MPa and 0.207 ± 0.018) compared to those of sLipo–Chol₅₀ (123.1 ± 11.9 MPa and 0.444 ± 0.032). This indicates that unsaturated lipids disrupt tight intermolecular interactions between lipid tails and add fluidity to the membrane. We further examined the colloidal stability of sLipo–Chol to study their compatibility with biological samples, here bird feces, generally collected from migratory stopover sites or infected birds for continuous surveillance of IAV (Figure S10, Supporting Information).^[41] The avian feces dispersed in phosphate-buffered saline were briefly centrifugated, and the supernatant solution was incubated with sLipo–Chol for 20 min, followed by incubation with sodium acetate buffer (0.3 M, pH 5.2) for 1 h. Interestingly, sLipo(u)–Chol₅₀ displayed a sudden increase in FRET ratio change, while three sLipo–Chol formulations showed resistance to fecal samples to some extent. Diverse compositions of fecal fluids likely contribute to the destabilization of unsaturated lipid membranes, as highlighted by the fact that avian feces contain nitrogenous waste (such as uric acid), gastrointestinal excrement (such as bile salts), and other insoluble components.^[42,43] Although cholesterol-containing unsaturated lipid membranes revealed highly deformable and fluidic

behavior, their structural stability was not sufficient for testing with complex biological samples. This implies that the appropriate selection of lipid compositions constituting sLipo–Chol nanosensors is critical for the sensitive and quantitative detection of IAV based on well-established FRET change signals and low interference from non-specific background signals.

We further optimized the assay buffer condition by varying concentrations of trypsin (0.5, 0.1, and 0.01 mg mL⁻¹) and sodium acetate (3, 1.5, and 0.3 M) in the acidic buffer and mixing them in an equal volume ratio (Figure S11, Supporting Information). Importantly, high concentrations of trypsin and the acidic buffer showed a high level of background signals in the assay buffer and moderate enhancement in the FRET signals with the activated virus. This differs from our expectation that more enzymes and sodium acetate salts would increase detection signals with enhanced fusion activity. We attribute this discrepancy to high ionic strength destabilizing sLipo–Chol in the assay buffer, leading to enhanced background signals and reduced relative FRET ratio changes. Thus, we selected an acidic buffer with 1.5 M of sodium acetate (pH 5.2) and 0.5 mg mL⁻¹ of trypsin to obtain maximal detection signals.

Having demonstrated the optimal conditions for the assay, we examined the detection performance of sLipo–Chol nanosensors with different cholesterol content to relate their detection ability to the mechanical properties of membranes, including membrane rigidity, fluidity, and permeability. The FRET ratio changes showed progressive increases for both sLipo–Chol₃₃ and sLipo–Chol₅₀. In contrast, the nonactivated virus and acidic buffer induced no significant FRET ratio changes for the three formulations (Figure 4a–c). Note that as the fusion progressed, the FRET signal change in the bulk fusion state gradually increased over 1 h, in contrast to the results of single-particle analysis (Figure 3). This inconsistent FRET kinetics between single-particle analysis and bulk readout is likely due to their different working principles. The single-particle approach uses TIRF to selectively light fluorophores at the sample's surface, revealing individual fused particles with high spatial resolution and sensitivity. This enables the identification of subtle changes in the FRET kinetics that may not be detectable with bulk FRET experiments using a plate reader that averages the fluorescence signals from the whole sample volume.^[44–47] Consequently, TIRF-based single-particle analysis allows the identification of fast kinetic events within a few minutes, while bulk reading using a plate reader counts FRET events over a longer time frame owing to its reduced sensitivity and spatial resolution.

Compared with the three nanosensors in the presence of activated viruses, the sLipo–Chol₅₀ nanosensor displayed the highest FRET ratio changes with the fastest responsiveness among the others (Figure 4d). This result is further supported by two kinetic parameters (maximum detection signal (%) and rate constant (K , min⁻¹)), obtained from an exponential curve fit of the FRET responses. As shown in Figure 4e, the maximum detection signal of sLipo–Chol₅₀ was estimated to be 21.79%, 1.4-fold higher than that of sLipo–Chol₃₃. The rate constant (K), which describes how rapidly the process occurs, was obtained to be 0.0832 and 0.2270 min⁻¹ for sLipo–Chol₃₃ and sLipo–Chol₅₀, respectively. Thus, the reduced membrane rigidity and increased fluidity of the sLipo–Chol₅₀ nanosensor led to a highly favorable sensing platform that enabled strong

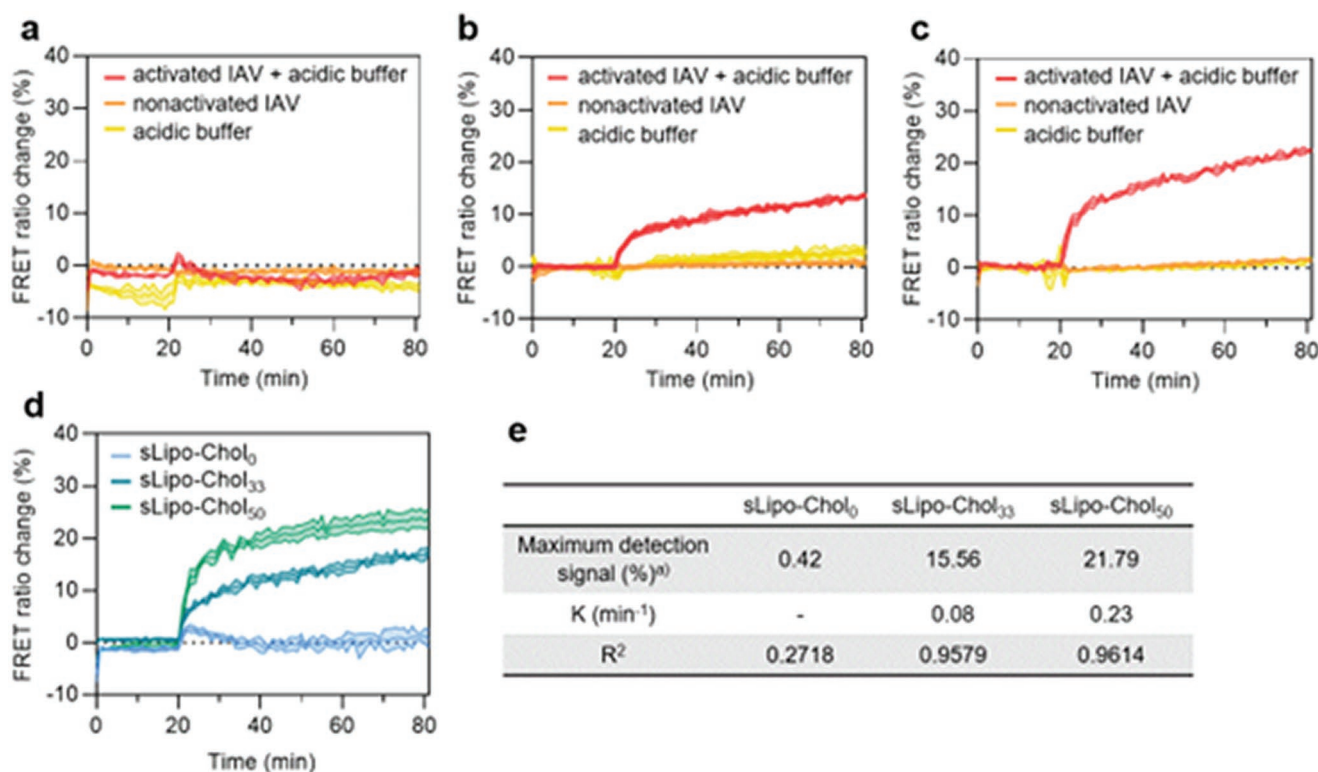


Figure 4. H9N2 IAV detection with various sLipo-Chol nanosensors. FRET ratio changes of a) sLipo-Chol₀, b) sLipo-Chol₃₃, and c) sLipo-Chol₅₀ nanosensors (0.05 mg mL⁻¹) incubated with activated viruses (10^{3.833} TCID₅₀ mL⁻¹, red) and an acidic buffer, nonactivated viruses (10^{3.833} TCID₅₀ mL⁻¹, orange), and an acidic buffer (yellow), respectively. The signals were monitored for 1 h after introducing the acidic buffer at $t = 20$ min. d) Comparison of FRET ratio responses of three sLipo-Chol nanosensors to the activated viruses under acidic pH. Data represents mean \pm standard deviation ($n = 3$). e) Summary of kinetic parameters of the FRET ratio changes of sLipo-Chol nanosensors in the presence of activated IAV obtained using a nonlinear fitting of the plateau, followed by a one-phase association model.

fluorescence by instantly responding to the target virus and was used for the subsequent specificity test. Therefore, modulating the unique features of nanosystems allows finely tuned, bio-inspired sensing platforms and guides to select the proper membrane composition of liposomal vesicles.

Our detection strategy involves sequential processes induced by specific reactions, such as binding of sialic acid to HA receptors, activation of HA with trypsin and low pH, and HA fusion peptide-assisted membrane fusion, enabling highly selective discrimination of IAV from other viruses. We assessed the specific detection of our nanosensors using seven subtypes of IAV (H1N3, H6N2, H1N2, H4N1, H6N1, H4N6, and CA04 (H1N1)) and other species of viruses, which were cultured in allantoic fluids or spiked in avian feces (Figure 5a). In addition to IAV, we tested three viruses that cause livestock infectious diseases, including porcine epidemic diarrhea virus (PEDV), canine distemper virus (CDV), and infectious canine hepatitis virus (ICHV), as control groups (see details of virus stock used in this study in Table S1, Supporting Information). As shown in Figure 5b, all IAV subtypes exhibited significantly enhanced FRET ratio changes only when the activated virus was treated with sLipo-Chol sensors. In contrast, disregarding virus activation and acidic buffer treatment, CDV, PEDV, and ICHV showed no discernible differences in signal generation. This result is due to the fact that CDV and PEDV require a different protease (e.g., furin) and receptor (e.g., porcine aminopeptidase

N) to fuse with host cells. Because ICHV is a nonenveloped icosahedral virus, it lacks a motif to interact with sLipo-Chol nanosensors.^[48,49]

Rapid and sensitive monitoring of fecal samples is essential to identify and isolate influenza infection-suspicious cases in animals and humans. However, the matrix of fecal samples is particularly complicated compared to nasal swabs, sputum, and allantoic fluids, making it difficult to sense the presence of the target virus directly using optical signal readouts. To validate the feasibility of the detection assay using fusogenic nanosensors, we used virus-spiked avian fecal samples. Prior to testing our sensors, the fecal samples containing different viruses were confirmed using qPCR (Table S2, Supporting Information), in which they were considered positive if the mean threshold cycle (C_t) value was obtained using IAV-targeting primers. We incubated known titers of activated or nonactivated viruses in avian feces for 1 h, briefly centrifuged them to remove excess contaminants, and used the supernatants for the assay. Consistent with the test results of allantoic virus stocks, only activated IAV groups with sLipo-Chol nanosensors caused statistically significant FRET signals compared to control viruses, in which the sLipo-Chol₅₀ nanosensor showed a 1.4-fold higher relative detection performance than sLipo-Chol₃₃ (Figure 5c). This suggests that the nanosensors presenting increased membrane permeability and responsiveness are preferred to detect IAVs with prominent fusion activity, consistent with the

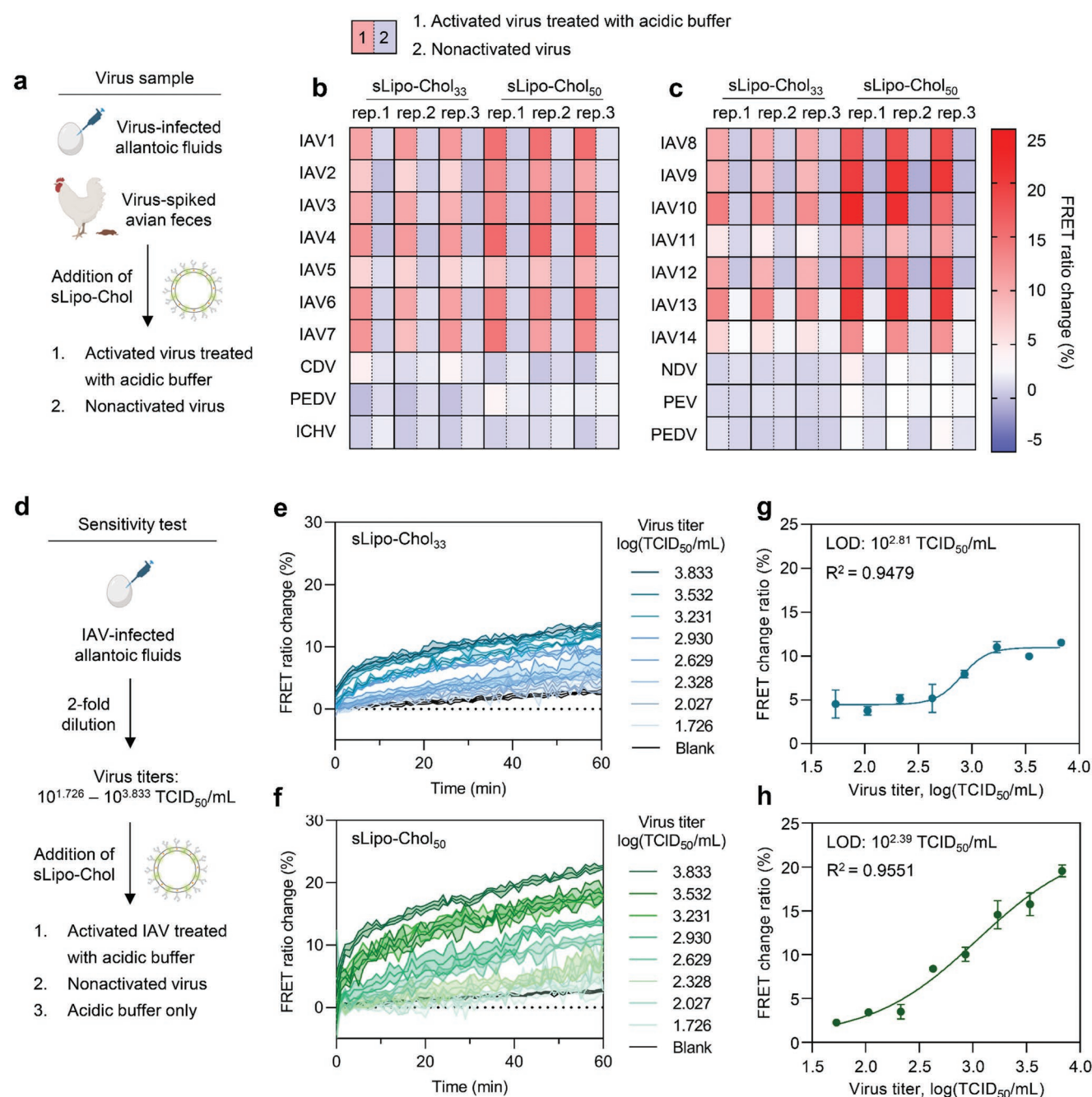


Figure 5. Specificity and sensitivity test of the sLipo-Chol nanosensors. a) Specificity test of the assay with sLipo-Chol with allantoic virus stocks and virus-containing avian fecal samples. Heatmap displaying FRET signal changes of sLipo-Chol₃₃ and sLipo-Chol₅₀ incubated with b) allantoic virus stocks and c) virus-containing fecal samples that were treated with trypsin and acidic buffer (data 1, left box) and nonactivated virus (data 2, right box). Influenza A virus, IAV; canine distemper virus, CDV; porcine epidemic diarrhea virus, PEDV; Infectious canine hepatitis virus, ICHV; Newcastle disease virus, NDV; porcine enterovirus, PEV. d) Sensitivity test of the assay with sLipo-Chol with IAV-infected allantoic fluids. e, f) Virus titer-dependent FRET signal change of sLipo-Chol₃₃ and sLipo-Chol₅₀ with the activated H9N2 virus ($10^{1.726} - 10^{3.833}$ TCID₅₀ mL⁻¹). g, h) Virus titer-dependent FRET signals at 30 min of incubation to assess the limit of detection (LOD) of each sLipo-Chol-based detection assay. Specificity and sensitivity tests were performed at 25 °C. Data represents mean \pm standard deviation ($n = 3$).

previous results in Figure 4 and the qPCR-based results. The FRET ratios of the nonactivated virus and acidic buffer only were negligible, indicating that the fecal samples rarely affected the stability of our nanosensors (Figure S12, Supporting Information). To further demonstrate the potential applicability of

the nanosensor to clinical samples, we examined the detection performance of sLipo-Chol₅₀ nanosensors by directly spiking IAVs into human saliva and serum (Figure S13, Supporting Information). The complexity and diversity of these biological matrices do not significantly impair the detection capability of

the nanosensor or lead to non-specific detection. Therefore, these results demonstrate efficient interactions of the designed sLipo-Chol nanosensors with activated viruses dispersed in complex matrices, allowing highly selective and simultaneous detection of a wide range of IAV subtypes among various infectious viruses.

Finally, we evaluated the detection sensitivity of the sLipo-Chol nanosensors using allantoic virus stocks of varying titers of H9N2 IAV from $10^{1.726}$ to $10^{3.833}$ TCID₅₀ mL⁻¹ (Figure 5d–h). The FRET ratio changes of sLipo-Chol nanosensors were recorded at 25 °C to produce a virus titer-response curve. The limit of detection (LOD) was calculated based on the three-sigma (3σ) method, providing the lowest virus titer that yields a signal three times higher than the standard deviation (σ) of the control. Notably, sLipo-Chol₅₀ nanosensors displayed a substantially wider dynamic range of detection and 2.6-fold enhancement in LOD, reaching signal saturation at higher virus titers than sLipo-Chol₃₃ (Figure 5e–h and Table S3, Supporting Information). This result showed the capability of sLipo-Chol₅₀ to interact with the activated IAV more competently than sLipo-Chol₃₃. The assay's sensitivity with sLipo-Chol₅₀ was further enhanced at 37 °C (Figure S14 and Table S3, Supporting Information). Overall, the obtained results confirmed that a fusogenic sLipo-Chol nanosensor-based detection assay allows simple and rapid detection of a fusion-competent virus within an hour, which compared favorably with other reported methods for IAV detection (Table S4, Supporting Information). Thus, understanding the molecular interaction of soft nanomaterials with enveloped viruses provides a valuable methodology for systematically designing a nanomaterial-based sensing system (i.e., tuning the mechanical properties of nanomaterials). In addition, this approach offers robustness against contaminants and inhibitors (avian feces, human serum, and saliva) and does not require sample pretreatments, such as thermal inactivation, chemical lysis, nucleic acid extraction and purification, enabling direct detection of viruses in biologically relevant samples. More importantly, nanosensors can detect the intact influenza virus that cannot be determined by immunoassays and qPCR, providing information on the infectivity of the collected samples.

3. Conclusion

The structural features and molecular interaction of IAV for infection provide valuable insights into developing biomimetic nanosensors that interact with viruses efficiently. We developed a fluorescent assay for selective and sensitive detection of IAV using fusogenic sLipo-Chol nanosensors. This nanosensor employs the FRET signal readouts produced from their rapid and specific membrane fusion with fusion competent IAV under a defined pH. The developed strategy represents the first demonstration of a biomimetic nanosensor that enables ratio-metric, quantitative fluorescence detection of IAV based on the control of mechanical properties for viral fusion. The design rationale lies in the IAV's fusion mechanism, where the HA proteins bind to the cellular sialic acid receptors and induce a conformational change of HA fusion peptides to merge two distinct viral and host membranes. Based on the critical influence

of mechanical properties on nano-bio interactions, we prepared sLipo-Chol nanosensors with tunable rigidity by introducing varying molar ratios of cholesterol into the membrane. Their membrane rigidity and fluidity were analyzed using AFM-based measurements of Young's modulus, FRAP studies, and the Laurdan-based assay, demonstrating that the increased cholesterol content in sLipo-Chol nanosensors caused an increase in membrane flexibility and softness. This feature relates to the enhanced responsiveness to viral fusion, accelerating fusion dynamics and instant FRET signal changes upon the addition of IAV. To study single-particle fusion kinetics, we applied TIRF-based FRET measurements and showed the nanosensor's ability to decoy and fuse the IAV through HA-mediated binding and low pH-triggered membrane fusion at the nanometer level. We also demonstrated that the prepared sLipo-Chol nanosensors exhibited highly selective and sensitive detection signals toward various subtypes of IAV, even in the avian fecal samples. This showed that the most responsive sLipo-Chol₅₀ nanosensor achieved the lowest LOD ($10^{2.39}$ and $10^{2.06}$ TCID₅₀ mL⁻¹ at 25 and 37 °C, respectively) while presenting low background signals. To extend this demonstration to other types and new variants of influenza viruses, the next step will be to evaluate the potential of the sLipo-Chol nanosensor to identify species specificity or mutation in HA. Indeed, the receptor-binding specificity of influenza viruses is determined by different sialic acid linkages, with avian and human influenza viruses known to favor $\alpha 2,3$ - and $\alpha 2,6$ -linked sialic acids, respectively.^[50] Mutations in the viral HA also alter receptor-binding preferences.^[51,52] Therefore, nanosensors with surfaces modified with $\alpha 2,3$ - or $\alpha 2,6$ -linked sialic acids could be utilized to distinguish between host types of IAVs or to differentiate between mutations in the HA. Additionally, as in immunoassays, the introduction of specific antibodies or aptamers into nanosensors can detect different subtypes of influenza viruses. Matching sialic acid with different linkages and multiple influenza-dependent fusion triggers (e.g., serine-based, or purine-based proteases) to the nanosensor will provide versatility and broad application of this nanosystem in influenza diagnostics. Thus, our findings underline the utmost importance of the bioinspired design of nanomaterials for efficient interaction with viruses and the modulation of their binding ability and membrane rigidity for enhanced detection performance. Our system presents an efficient method for the quantitative detection of intact IAV in samples without RNA extraction and purification, ranging from protein-rich biological fluids to complicated matrices, holding immense potential for fast detection and response to life-threatening emerging infectious viruses.

4. Experimental Section

Materials: All phospholipids, including DSPC (18:0 PC, 1,2-distearoyl-*sn*-glycero-3-phosphocholine), DSPS (18:0 PS, 1,2-distearoyl-*sn*-glycero-3-phospho-L-serine), DSPE-PEG (1,2-distearoyl-*sn*-glycero-3-phosphoethanolamine-*N*-[carboxy(polyethylene glycol)4]), total ganglioside (TG) extracts (from the porcine brain), DSTAP (18:0 TAP, 1,2-stearoyl-3-trimethylammonium-propane), DOPC (18:1 PC, 1,2-dioleoyl-*sn*-glycero-3-phosphocholine), and DOPS (18:1 PS, 1,2-dioleoyl-*sn*-glycero-3-phospho-L-serine) were purchased from Avanti Polar Lipids (AL, USA). A cellulose ester (CE) membrane (Spectra/Por® Biotech CE Tubing, MWCO 10 kDa) was purchased from

Spectrum Labs (CA, USA), and SM-2 Bio-Beads™ were purchased from Bio-Rad (CA, USA). Hydroxyethyl piperazine ethane sulfonic acid (HEPES), potassium chloride, trypsin from bovine pancreas, sodium acetate buffer solution (pH 5.2), Triton X-100, N-(2-aminoethyl)-3-aminopropyltrimethoxysilane, and sodium bicarbonate (NaHCO₃) were purchased from Sigma-Aldrich (MO, USA). Methoxy polyethylene glycol-succinimidyl valerate (mPEG-SVA, MW 5 kDa) and biotin-PEG (MW 5 kDa) were obtained from Laysan Bio Inc. (AL, USA). 3,3',3'',3'''-Diiodododecylcarboxyanine perchlorate (DiO), 1,1''-diiodododecyl-3,3,3',3'''-tetramethylindocarbocyanine perchlorate (DiI), 1,1''-diiodododecyl-3,3,3',3'''-tetramethylindocarbocyanine 4-chlorobenzenesulfonate salt (DiD), Oregon Green™ 488 1,2-dihexadecanoyl-sn-glycero-3-phosphoethanolamine (DHPE), and Laurdan (6-dodecanoyl-2-dimethylaminonaphthalene) probe were purchased from ThermoFisher Scientific (MA, USA). All other chemicals and reagents with analytical grade were used without further purification unless otherwise stated. The 400-mesh copper grids with formvar and carbon support films and the highest grade VI AFM mica discs were purchased from Ted Pella, Inc. (CA, USA). AFM probes with soft silicon nitride cantilever with silicon nitride tips (MSCT) were purchased from Bruker (MA, USA). Soluble HA protein (A/Hong Kong/483/97 H5N1) and rapid H5 avian influenza virus (AIV) antigen test kit was purchased from ACRO Biosystems (DE, USA) and Gentaur Molecular Products (Belgium), respectively.

Preparation of sLipo-Chol with Various Cholesterol Contents: The sialic acid-presenting lipid vesicles (sLipo-Chol) were prepared based on the thin film hydration and extrusion method. First, lipid mixtures composed of DSPC, DSPS, DSPE-PEG, TG, and cholesterol were dissolved in 150 µL of chloroform in a round-bottom flask. The molar ratio of DSPC:DSPS:DSPE-PEG:TG was 1:1:0.15:0.06, and cholesterol varied from 0, 1.1, and 2.2 to prepare sLipo-Chol₀, sLipo-Chol₃₃, and sLipo-Chol₅₀, respectively. For the preparation of sLipo-Chol nanosensors (FRET pair dyes-encapsulated sLipo-Chol), the lipid mixture was combined with 10 µg of FRET dyes (DiO donor and DiI acceptor or DiI donor and DiD acceptor) in chloroform. Chloroform was evaporated entirely using a rotary evaporator under reduced pressure to make a thin film, followed by hydration with HEPES buffer (20 mM HEPES, 100 mM KCl; pH 7.5) overnight at 4 °C. After sonication for 1 h, the homogeneous lipid suspensions were passed 51 times through a 100 nm pore size polycarbonate membrane using a minietruder (Avanti Polar Lipids), providing monodisperse unilamellar liposomes. The sonication and extrusion were performed at 50 °C for sLipo-Chol₀, and at room temperature otherwise. The resulting liposome solution was dialyzed overnight with HEPES buffer containing 4 g of pre-cleaned SM-2 Bio-Beads™ to remove excess fluorescent dye molecules.

Characterization of sLipo-Chol: The hydrodynamic size and zeta potential of sLipo-Chol were measured by dynamic light scattering (DLS) at 25 °C (ELS-Z2000ZS, Otsuka Electronics, Japan). The sLipo-Chol solution (0.05 mg mL⁻¹) was diluted 20-fold with distilled water, and measurements were carried out in triplicate for each sample. The morphologies of sLipo-Chol were observed using JEM-F200 transmission electron microscopes (TEM; JEOL, Japan) at an accelerating voltage of 120 kV. The samples were prepared by placing 10 µL of sLipo-Chol dispersion on the formvar/carbon-coated 400-mesh copper grids, negatively stained using a 3% (w/v) aqueous neutral solution of phosphotungstic acid, and dried overnight prior to imaging.

Analysis of Topography and Young's Modulus Using AFM: For atomic force microscopy (AFM)-based nanoindentation and topography studies, samples were prepared by 5 min incubation of sLipo-Chol on freshly cleaved mica. Following the incubation, unbound sLipo-Chol were removed by successive washes with distilled water. AFM imaging and force measurements were carried out using an NX-10 microscope (Park Systems, South Korea) equipped with a silicon cantilever probe with a spring constant of 0.07 N m⁻¹ (MSCT, Bruker, Germany). The AFM images were recorded in contact mode with a scan rate of 1 Hz. All force-indentation depth curve measurements were performed by manipulating the cantilever at a velocity of 50 nm s⁻¹. Before measuring samples, the cantilever deflection and photovoltage ratio were calibrated on the bare mica substrate. To obtain the data on the elastic behavior of sLipo-Chol,

the indentation depth of pressing the cantilever was maintained at less than 5 nm. For each sLipo-Chol, six independent experiments with different samples were conducted, and the obtained force curves were analyzed into Young's modulus using the Hertzian model through an image processor XEI Park Systems software.

FRAP Experiments Using Supported Lipid Bilayer of sLipo-Chol: Fluorescence recovery after photobleaching (FRAP) experiments were conducted with a Zeiss LSM 980 confocal microscope (Zeiss, Germany) equipped with a 63× oil immersion objective and 1.4 numerical aperture (NA) (Zeiss Plan-Apochromat). A fluorescent lipid, Oregon Green 488 DHPE (Oregon-DHPE), was added to the lipid mixtures at a molar ratio of DSPC:DSPS:Oregon-DHPE:DSPE-PEG:TG = 1:1:0.02:0.15:0.06 to make fluorescently labeled sLipo-Chol. The supported lipid bilayer on a sterile confocal dish was prepared by incubating sLipo-Chol solution (0.1 mg mL⁻¹) with 10 kDa PEG solution at 60 °C for 30 min and slowly cooling to room temperature.^[25] After incubation, the excess solution was rinsed by gentle stirring with Dulbecco's phosphate buffered saline (DPBS) at least five times. The fluorescence image was obtained with a 488 nm laser (image size: 512 × 512 pixels), and a scanning mode was used to bleach a circle area with a diameter of 10 µm at 100% laser power. The fluorescence recovery was regularly imaged with a scanning speed of 1 s frame⁻¹. The fluorescence intensity change over time was fit using a one-phase association model (GraphPad Prism 9.0) to calculate a diffusion coefficient (*D*) with the equation $D = w^2 / 4t_{1/2}$, where *w* is the radius of the photobleached area, and *t*_{1/2} is the time required for half recovery of the maximum fluorescence intensity.

Laurdan Assay: The Laurdan assay was conducted using 1 mM of Laurdan solution in dichloromethane as a stock solution. After dilution into 10 µm with distilled water, the Laurdan solution was incubated with an equal volume of sLipo-Chol solutions (50 µm of lipids) for 1 h. The Laurdan-treated samples were excited at 340 nm, and the emission spectra were recorded from 400 to 600 nm using a Spectra Max® i3x microplate reader (Molecular Devices, CA, USA). For the estimation of lipid membrane ordering, the generalized polarization (GP) value was calculated from the emission spectra according to the following equation, $GP = (I_{450} - I_{510}) / (I_{450} + I_{510})$, where *I*₄₅₀ and *I*₅₁₀ indicate emission intensity at 450 and 510 nm, respectively.

Solubilization Assay: The solubilization assay was performed using a nonionic surfactant Triton X-100 (Tx-100) to destabilize the membrane of sLipo-Chol with various rigidities. The assay was carried out by incubating the sLipo-Chol nanosensors (0.05 mg mL⁻¹) with an equivalent volume of 10% (v/v) Tx-100 for 1 h at 25 °C. The fluorescence intensities of DiO and DiI dyes emitted at 504 and 574 nm were recorded using a Spectra Max® i3x microplate reader with excitation at 475 nm. The FRET ratio was defined as the relative fluorescence intensity of DiI normalized to the total fluorescence intensity ($FRET\ ratio = F_{DiI} / F_{I_{total}}$, where $F_{I_{total}} = F_{DiO} + F_{DiI}$, and *F*_{DiO} and *F*_{DiI} were the fluorescence intensities of DiO and DiI dyes at 504 and 574 nm, respectively).

Preparation of Virus Stocks and Fecal Samples: The influenza A viruses (IAV) with various subtypes, including H1N1, H1N3, H3N2, H3N6, H4N4, H4N6, H6N1, and H6N2, and Newcastle disease virus (NDV), were propagated in the allantoic cavity of 11-day-old embryonated chicken eggs. Each virus stock (100 µL) was inoculated into the allantoic cavities of chicken eggs. After a 72 h incubation at 37 °C, the eggs were chilled overnight at 4 °C. The allantoic fluids containing the propagated viruses were harvested and purified by centrifugation at 4,000 rpm for 20 min. The supernatants were transferred to new test tubes and frozen at -80 °C for long-term storage. Porcine epidemic diarrhoea virus (PEDV), porcine enterovirus (PEV), and canine distemper virus (CDV) were propagated in Vero cells, and infectious canine hepatitis virus (ICHV) was propagated in Madin-Darby canine kidney (MDCK) cells. After 72 h incubation at 37 °C, the cells were chilled overnight at 4 °C. The supernatant containing the propagated viruses was collected and purified by centrifugation at 4,000 rpm for 20 min, transferred to new test tubes, and frozen at -80 °C for long-term storage. The prepared virus stocks were used directly for the assay.

Fecal samples were collected from a stopover site of wild migratory aquatic birds in South Korea. For the virus detection assay, the equivalent

volume of a virus stock was spiked into feces suspension in DPBS. After 1 h of incubation, the supernatant solution was transferred to a new test tube and briefly centrifuged (8000 rpm, 5 min) to remove residual feces or other contaminants. The prepared fecal samples containing viruses were confirmed by quantitative reverse transcription polymerase chain reaction (RT-qPCR) using the Qiagen One-Step RT-PCR kit according to the manufacturer's instructions. Viral RNA was extracted using the QiAamp Viral RNA Mini kit according to the manufacturer's instructions. Subsequently, 25 μL of the total reaction mixture was prepared by adding RNA extracts (5 μL) to the master mix (20 μL) containing forward/reverse primers, probes, enzymes, and dNTP mix. Then qRT-PCR was performed as follows: 50 $^{\circ}\text{C}$ for 30 min for reverse transcription, 95 $^{\circ}\text{C}$ for 15 min for polymerase activation, 40 cycles of denaturation at 94 $^{\circ}\text{C}$ for 30 s, annealing at 55 $^{\circ}\text{C}$ for 30 s, and extension at 72 $^{\circ}\text{C}$ for 1 min. The primer and probe sequences targeting the M gene are as follows: forward primer, 5' GAC CRA TCC TGT CAC CTC TGA C 3'; reverse primer, 5' AGG GCA TTY TGG ACA AAK CGT CTA 3'; and probe, 5' FAM-TGC AGT CCT CGC TCA CTG GGC ACG-BHQ1 3'.

Confocal Microscopy Imaging: For confocal microscopy imaging, the sLipo-Chol nanosensor and IVA were stained with DiO and DiI, respectively. DiO-labeled sLipo-Chol was prepared using the thin film hydration method as described previously. The IVA was stained by incubation with 10 μL of DiI solution (1 mg mL^{-1} in dimethyl sulfoxide) for 30 min, and free dyes were removed by Vivaspin ultrafiltration units (MWCO 10 kDa). The DiI-labeled IVA ($10^{3.833}$ TCID₅₀ mL^{-1}) was activated by treatments with 20 μL of trypsin solution (0.5 mg mL^{-1}) for 20 min, followed by incubation with DiO-labeled sLipo-Chol nanosensors (0.05 mg mL^{-1}) and sodium acetate buffer (1.5 M, pH 5.2) for 30 min at 25 $^{\circ}\text{C}$. The sample solution (20 μL) was pipetted onto the pre-cleaned slide glass, covered with a cover glass, and imaged using the LSM 980 confocal laser scanning microscope (Zeiss, Germany) equipped with a 63 \times oil immersion objective with a NA of 1.4.

Cryo-TEM Imaging: For cryogenic TEM (cryo-TEM) imaging, 3 μL of sLipo-Chol₅₀ (1 mg mL^{-1}) or sLipo-Chol₅₀ with the activated IVA ($10^{3.833}$ TCID₅₀ mL^{-1}) was loaded onto freshly glow-discharged UltrAuFoil R1.2/1.3 300-mesh grids (Quantifoil Micro Tools GmbH), followed by plunge freezing using a Vitrobot Mark IV system (ThermoFisher Scientific) at 100% relative humidity and 4 $^{\circ}\text{C}$. Image data were collected using a Talos Arctica G2 TEM (ThermoFisher Scientific) in the Korea Basic Science Institute (KBSI), operating at 200 kV acceleration voltage in parallel illumination conditions. Images were acquired in an energy-filtered TEM (EF TEM) mode with a slit width of 20 eV using a BioQuantum energy filter and a K3 direct electron detector (Gatan Inc.) at a nominal magnification of 63 000 \times corresponding to a calibrated pixel size of 1.36 \AA per pixel with a spot size of a 4 and 50 μm C2 aperture. Data collection was performed using EPU software (ThermoFisher Scientific), and exposures were recorded at a defocus range of -3.5 μm in electron counting mode for 3.0 s at a dose rate of 18.6 e^{-} pixel $^{-1}$ s $^{-1}$ resulting in a total dose of 30 e^{-} \AA^{-2} .

Single-Particle FRET Analysis Using TIRF Microscopy: For single-particle total internal reflection fluorescence (TIRF) microscopy analysis, the substrate was passivated by a series of steps reported elsewhere.^[53] Briefly, the coverslips and pre-drilled quartz slides were cleaned with acetone, and the surface was activated by sonication in 1 M potassium hydroxide for 1 h. The surface was further functionalized with amine groups using N-(2-aminoethyl)-3-aminopropyltrimethoxysilane via silane chemistry. Subsequently, a mixture containing 49 mg of mPEG-SVA (MW 5 kDa) and 1 mg of biotin-PEG (MW 5 kDa) in fresh 0.1 M sodium bicarbonate solution was dispensed (70 μL) onto the air-dried slides and the coverslips and incubated for 4 h. The PEGylated slides and coverslips were washed with distilled water and air-dried thoroughly and stored at -20 $^{\circ}\text{C}$ for further use.

The PEGylated quartz slide and coverslip were assembled into an array of flow chambers with a volume of 20 μL . The biotinylated sLipo-Chol₅₀ nanosensors labeled with DiI (0.05 mg mL^{-1}) were immobilized on the surface of the flow chamber using a neutravidin-biotin coupling. After introducing DiD-labeled IVA ($10^{2.833}$ TCID₅₀ mL^{-1}) into the flow chamber and incubating for 20 min, the acidic buffer (150 mM sodium acetate,

pH 5.2) was subsequently added to induce fusion between nanosensors and IVA. After each addition, the chambers were washed extensively with phosphate-buffered saline. All incubations were performed at room temperature unless otherwise stated. Fluorescent images were taken using an inverted Nikon Eclipse Ti2 microscope implemented with an objective-based TIRF configuration, including an H-TIRF module and an electron-multiplying charge-coupled device (EMCCD; Andor iXon Life888). The microscope was equipped with a perfect focus system with an oil immersion objective (Apo TIRF 60 \times objective lens with NA of 1.49). Each molecule was illuminated with laser excitations at 541 and 640 nm and customized optical filter sets (purchased from Chroma, Inc.) for the donor (DiI) and acceptor fluorophores (DiD), respectively. The single-particle FRET study was analyzed by a custom MATLAB (R2019b) code to determine the counts, intensities, and size of each channel's coordinates. The FRET ratios (E) were determined for tested groups with the formula: $E = I_A / (I_A + I_D)$, where I_D and I_A are background-corrected intensities of the donor and acceptor, respectively. The spot area in TIRF imaging was measured using a thresholding and segmentation process, and then the spots were sorted according to intensity. The intensities were linked based on the centroid position and normalized to find the spot area using the customized MATLAB code.

IVAV Detection Using sLipo-Chol Nanosensors: The detection assay using sLipo-Chol nanosensors was carried out by treating with the activated or nonactivated virus solution. The viruses were activated by incubating 20 μL of viruses with various titers ($10^{1.726}$ – $10^{3.833}$ TCID₅₀ mL^{-1} of H9N2 IVA and other viruses listed in Tables S2 and S3, Supporting Information) with 20 μL of trypsin (0.5 mg mL^{-1}) for 20 min to initiate a proteolytic cleavage of the HA fusion protein. The activated viruses were then incubated with 40 μL of sLipo-Chol nanosensor solution (0.05 mg mL^{-1}), followed by subsequent addition of 1.5 M sodium acetate buffer (pH 5.2) to induce conformational changes of the HA. Treatments with inactivated viruses and acidic buffer were used as controls. The fluorescence emission spectra were monitored for 1 h at 25 $^{\circ}\text{C}$ using a Spectra Max® i3x microplate reader with excitation at 475 nm and emission at 504–599 nm.

The FRET ratio change (or the detection signal) of individual sLipo-Chol nanosensors in the presence or absence of activated viruses was calculated using the equation below. The FRET ratio (R) was defined as the relative fluorescence intensity of an acceptor normalized to the total fluorescence intensity. The minimum FRET ratio (R_{\min}) was obtained from the FRET ratio of sLipo-Chol nanosensors treated with 10% (v/v) Triton X-100. In the equation below, R_x and R_{dw} refer to the relative FRET ratios of the sLipo-Chol nanosensors under a given condition and in deionized water, respectively.

$$\text{FRET ratio change (\%)} = \frac{R_{\text{dw}} - R_x}{R_{\text{dw}} - R_{\min}} \times 100 \quad (1)$$

Supporting Information

Supporting Information is available from the Wiley Online Library or from the author.

Acknowledgements

C.P. and E.K. contributed equally to this work. E. Kim acknowledges support from the National Research Foundation of Korea (NRF) grant funded by the Korea government (MSIT) (No. 2022R1C1C1005390). B. C. Kim acknowledges support from the Basic Science Research Program through the National Research Foundation of Korea (NRF) grant funded by the Ministry of Education (No. 2022R111A1A01068195). D. Song acknowledges support from the National Research Foundation of Korea (NRF) grant funded by the Korea government (MSIT) (No. 2021M3E5E3080556). S. Haam acknowledges support from the Bio

& Medical Technology Development Programs of the NRF funded by MSIT (No. 2021M3E5E3080565) and Korea Environment Industry & Technology Institute (KEITI) through Technology Development Project for Biological Hazards Management in Indoor Air Program, funded by Korea Ministry of Environment (MOE) (RE202101004).

Conflict of Interest

The authors declare no conflict of interest.

Author Contributions

C. Park and E. Kim contributed equally to this work.

Data Availability Statement

The data that support the findings of this study are available from the corresponding author upon reasonable request.

Keywords

fusogenic sensors, host cell-mimic systems, influenza A virus detection, membrane rigidity, viral membrane fusion

Received: December 14, 2022

Revised: April 13, 2023

Published online: April 29, 2023

- [1] D. E. Bloom, D. Cadarette, *Global Health: Ethical Challenges*, Cambridge University Press, Cambridge **2021**.
- [2] S. Jiang, Z.-L. Shi, *Virol Sin* **2020**, *35*, 263.
- [3] E. Kim, E. K. Lim, G. Park, C. Park, J. W. Lim, H. Lee, W. Na, M. Yeom, J. Kim, D. Song, S. Haam, *Adv. Mater.* **2021**, *33*, 2005927.
- [4] E. Surkova, V. Nikolayevskiy, F. Drobniowski, *Lancet Respir Med* **2020**, *8*, 1167.
- [5] Y. Yamaoka, S. S. Jeremiah, K. Miyakawa, R. Saji, M. Nishii, I. Takeuchi, A. Ryo, *Clin. Infect. Dis.* **2020**, *72*, 1291.
- [6] Z. Qin, R. Peng, I. K. Baravik, X. Liu, *Matter* **2020**, *3*, 628.
- [7] A. Arima, I. H. Harlisa, T. Yoshida, M. Tsutsui, M. Tanaka, K. Yokota, W. Tonomura, J. Yasuda, M. Taniguchi, T. Washio, *J. Am. Chem. Soc.* **2018**, *140*, 16834.
- [8] A. S. Peinetti, R. J. Lake, W. Cong, L. Cooper, Y. Wu, Y. Ma, G. T. Pawel, M. E. Toimil-Molares, C. Trautmann, L. Rong, *Sci. Adv.* **2021**, *7*, eabh2848.
- [9] R. A. Bull, T. N. Adikari, J. M. Ferguson, J. M. Hammond, I. Stevanovski, A. G. Beukers, Z. Naing, M. Yeang, A. Verich, H. Gamaarachchi, *Nat. Commun.* **2020**, *11*, 6272.
- [10] M. Kielian, F. A. Rey, *Nat. Rev. Microbiol.* **2006**, *4*, 67.
- [11] W. Weissenhorn, A. Hinz, Y. Gaudin, *FEBS Lett.* **2007**, *581*, 2150.
- [12] L. Nathan, A. L. Lai, J. K. Millet, M. R. Straus, J. H. Freed, G. R. Whittaker, S. Daniel, *ACS Infect. Dis.* **2019**, *6*, 250.
- [13] E. K. Punch, S. Hover, H. T. Blest, J. Fuller, R. Hewson, J. Fontana, J. Mankouri, J. N. Barr, *J. Biol. Chem.* **2018**, *293*, 9937.
- [14] T. Tang, A. Savva, W. C. Traberg, C. Xu, Q. Thiburce, H.-Y. Liu, A.-M. Pappa, E. Martinelli, A. Withers, M. Cornelius, *ACS Nano* **2021**, *15*, 18142.
- [15] L. V. Chernomordik, M. M. Kozlov, *Nat. Struct. Mol. Biol.* **2008**, *15*, 675.
- [16] S.-T. Yang, A. J. Kreutzberger, J. Lee, V. Kiessling, L. K. Tamm, *Chem. Phys. Lipids* **2016**, *199*, 136.
- [17] F. J. Byfield, H. Aranda-Espinoza, V. G. Romanenko, G. H. Rothblat, I. Levitan, *Biophys. J.* **2004**, *87*, 3336.
- [18] X. Sun, G. R. Whittaker, *J. Virol.* **2003**, *77*, 12543.
- [19] Y. Takechi-Haraya, K. Sakai-Kato, Y. Abe, T. Kawanishi, H. Okuda, Y. Goda, *Langmuir* **2016**, *32*, 6074.
- [20] A. V. R. Murthy, F. Guyomarc'h, C. Lopez, *Langmuir* **2016**, *32*, 6757.
- [21] D. Drabik, G. Chodaczek, S. Kraszewski, M. Langner, *Langmuir* **2020**, *36*, 3826.
- [22] D. Vorselen, M. C. Piontek, W. H. Roos, G. J. Wuite, *Front. Mol. Biosci.* **2020**, *7*, 139.
- [23] H. Wu, M. Yu, Y. Miao, S. He, Z. Dai, W. Song, Y. Liu, S. Song, E. Ahmad, D. Wang, *Acta Pharm. Sin. B* **2019**, *9*, 858.
- [24] C. Lubrano, U. Bruno, C. Ausilio, F. Santoro, *Adv. Mater.* **2022**, *34*, 2110194.
- [25] A. Berquand, P.-E. Mazeran, J. Pantigny, V. Proux-Delrouyre, J.-M. Laval, C. Bourdillon, *Langmuir* **2003**, *19*, 1700.
- [26] D. Soumpasis, *Biophys. J.* **1983**, *41*, 95.
- [27] D. Beckers, D. Urbancic, E. Sezgin, *J. Phys. Chem. B* **2020**, *124*, 1487.
- [28] K. Scheinpflug, O. Krylova, H. Strahl, in *Antibiotics: Methods and Protocols* (Ed: P. Sass), Springer, New York **2017**.
- [29] T. Parasassi, G. De Stasio, G. Ravagnan, R. Rusch, E. Gratton, *Biophys. J.* **1991**, *60*, 179.
- [30] C. Park, J.-W. Lim, G. Park, H.-O. Kim, S. Lee, Y. H. Kwon, S.-E. Kim, M. Yeom, W. Na, D. Song, E. Kim, S. Haam, *J. Mater. Chem. B* **2021**, *9*, 9658.
- [31] N. Deo, P. Somasundaran, *Langmuir* **2003**, *19*, 2007.
- [32] H. Heerklotz, *Q. Rev. Biophys.* **2008**, *41*, 205.
- [33] B. S. Hamilton, G. R. Whittaker, S. Daniel, *Viruses* **2012**, *4*, 1144.
- [34] P. Mühlenbrock, M. Sari, C. Steinem, *Eur. Biophys. J.* **2021**, *50*, 239.
- [35] T.-Y. Yoon, B. Okumus, F. Zhang, Y.-K. Shin, T. Ha, *Proc Natl Acad Sci U S A* **2006**, *103*, 19731.
- [36] E. Böttcher, T. Matrosovich, M. Beyerle, H.-D. Klenk, W. Garten, M. Matrosovich, *J. Virol.* **2006**, *80*, 9896.
- [37] C. Chaipan, D. Kobasa, S. Bertram, I. Glowacka, I. Steffen, T. Solomon Tsegaye, M. Takeda, T. H. Bugge, S. Kim, Y. Park, *J. Virol.* **2009**, *83*, 3200.
- [38] D. A. Steinhauer, *Virology* **1999**, *258*, 1.
- [39] J. K. Taubenberger, *Proc Natl Acad Sci U S A* **1998**, *95*, 9713.
- [40] A. Kuch, E. Csonka, *Acta Microbiol* **1957**, *4*, 357.
- [41] J.-H. Nam, E. España, E.-J. Song, S.-M. Shim, W. Na, S.-H. Jeong, J. Kim, J. Jang, D. Song, J.-K. Kim, *Sci. Rep.* **2021**, *11*, 8002.
- [42] K. S. Islam, S. Fukiya, M. Hagio, N. Fujii, S. Ishizuka, T. Ooka, Y. Ogura, T. Hayashi, A. Yokota, *Gastroenterology* **2011**, *141*, 1773.
- [43] P. Eriksson, E. Mourkas, D. González-Acuna, B. Olsen, P. Ellström, *Infect Ecol Epidemiol* **2017**, *7*, 1386536.
- [44] L. Wessels, M. W. Elting, D. Scimeca, K. Weninger, *Biophys. J.* **2007**, *93*, 526.
- [45] J. M. Hernandez, A. J. Kreutzberger, V. Kiessling, L. K. Tamm, R. Jahn, *Proc. Natl. Acad. Sci. USA* **2014**, *111*, 12037.
- [46] V. Kiessling, B. Liang, L. K. Tamm, *Methods Cell Biol* **2015**, *128*, 339.
- [47] M. E. Bowen, K. Weninger, A. T. Brunger, S. Chu, *Biophys. J.* **2004**, *87*, 3569.
- [48] V. Von Messling, D. Milosevic, P. Devaux, R. Cattaneo, *J. Virol.* **2004**, *78*, 7894.
- [49] W. Li, F. J. van Kuppeveld, Q. He, P. J. Rottier, B.-J. Bosch, *Virus Res.* **2016**, *226*, 117.
- [50] J. E. Stencel-Baerenwald, K. Reiss, D. M. Reiter, T. Stehle, T. S. Dermody, *Nat. Rev. Microbiol.* **2014**, *12*, 739.
- [51] C. J. Russell, R. G. Webster, *Cell* **2005**, *123*, 368.
- [52] K. Shinya, M. Ebina, S. Yamada, M. Ono, N. Kasai, Y. Kawaoka, *Nature* **2006**, *440*, 435.
- [53] B. Hua, K. Y. Han, R. Zhou, H. Kim, X. Shi, S. C. Abeyisirigunawardena, A. Jain, D. Singh, V. Aggarwal, S. A. Woodson, *Nat. Methods* **2014**, *11*, 1233.